Investigating Complex Geometrical Features in LPBF-Produced Parts: A Material-Based Comparison Between Different Titanium Alloys

Metals and Materials International
https://doi.org/10.1007/s12540-023-01460-4

# Investigating Complex Geometrical Features in LPBF-Produced Parts: A Material-Based Comparison Between Different Titanium Alloys

**A. Carrozza[1,2] · B. A. Bircher[3] · A. Aversa[2,4] · S. Biamino[2,4]**

Received: 9 March 2023 / Accepted: 26 April 2023


**Abstract**
The Ti–6Al–4V (Ti64) alloy is a well-established material to be processed via laser powder bed fusion (LPBF). Recently, other α + β titanium alloys are receiving attention, such as Ti–6Al–2Sn–4Zr–6Mo (Ti6246). Their typical industrial fields of application (aerospace, automotive), often require critical design choices, such as low wall thicknesses and hollow channels. Thus, a comparative analysis between these two competitor alloys in terms of processability was conducted in this work. To do so, specific sample designs were developed. The specimens were analyzed in terms of geometrical compliance with the initial design, porosity, and microstructure. A correlation between the width of the specimens and their porosity, microstructure and hardness was found. Overall, both the alloys proved to be well processable, even for very low wall thickness (300 µm) and channel diameter (1 mm) values. Nevertheless, the Ti6246 alloy seemed to behave better in specific scenarios. For instance, some Ti64 specimens provided delamination. The hollow channels proved to be challenging for both materials, mainly due to the high amount of residual powder particles adhered to the upper part of the holes. This works aims at giving a materials perspective on process-related issues, considering the LPBF-induced defectology and microstructural variations in these Ti alloys.

**Keywords** Additive manufacturing · Laser powder bed fusion · Design · Titanium · Thin wall · Processability

## 1 Introduction

Additive manufacturing (AM) technologies are a hot topic nowadays due to numerous reasons, such as low materials waste, high customizability of components and the potential to manufacture very intricate shapes. Among these technologies, laser powder bed fusion (LPBF or PBF-LB) has been a well-established technique for a decade. LPBF techniques are very promising when dealing with complex and minute designs, mainly due to the low particle size of the feedstock powder and the possibility to generate very small melt pools [1]. However, the avoidance of process-related defects (e.g., distortion, porosity) requires a strict optimization of the process parameters (e.g., laser power, scanning speed).

Since intricate designs are one of the most important advantages granted by the LPBF technology, the relative limitations of the manufacturing process are fundamental to assess. This is particularly important considering that lightweight structures are usually very complex from a geometrical point of view [2]. One of the most complex geometries to handle are usually parts characterized by a very low wall thickness. Wu et al. [3] investigated this limitation in different LPBF-processed materials, concluding that the minimum thickness achievable is severely limited by the typical high colling rates developed during the process, which result in thermal shrinkage and residual stress accumulation, thus making the outcome alloy-dependent. Moreover, the process parameters optimization is usually carried out on bulk parts. Thus, the resulting process maps are not applicable for thin-walled structures, due to the different thermal conditions locally occurring. These conditions can cause variations in the consolidation (pores, cracks, geometrical accuracy) and microstructural features and properties. Chen et al. [4] used

✉ A. Carrozza
alessandro.carrozza@unibg.it

1 Department of Engineering and Applied Sciences, University of Bergamo, Dalmine, BG, Italy

2 National Interuniversity Consortium of Materials Science and Technology (INSTM), Firenze, Italy

3 Laboratory for Length, Nano- and Microtechnology, Federal Institute of Metrology (METAS), Bern-Wabern, Switzerland

4 Department of Applied Science and Technology, Politecnico di Torino, Torino, Italy

Published online: 27 May 2023

an analytical and experimental approach to investigate the geometrical compliance of LPBF-produced Ti64 structures. The authors found that the maximum displacement can be found at half the height of the thin wall. However, a stable shape is achieved after a threshold height is reached, due to the combined contributions of the material contraction and constrain from the baseplate. Recently, Kushwaha et al. [5] investigated the microstructure, hardness and wear behavior of thin-walled LPBF-manufactured Ti64 specimens. Significant material inhomogeneity was observed, resulting from the microstructure being significantly coarser in the bottom region of the parts.

Parts with horizontal channels are also problematic to manufacture. This is mainly due to possible local collapse of the upper part of the hole, related to the lack of material underneath to sustain the weight of the upper layer. Furthermore, the geometrical accuracy of such parts is usually rather low because of the thermal shrinkage [6]. Avoiding in-process failure and improving the geometrical accuracy of the parts are the reason why several design guidelines specific for AM exist. For instance, Kranz et al. [7] suggested the necessity to adopt support structures inside holes > 12 mm to prevent the collapse of Ti64 structures, but no recommendations regarding small channels were provided. In fact, most literature focuses on the maximum size achievable in bulk parts [8, 9]. Nevertheless, the lower dimensional limit of horizontal channel in LPBF-processed parts is also a critical aspect to consider. In fact, these features show a tendency to clog with residual/partially sintered powder. This phenomenon might be critical in terms of design constraints and de-powdering operations [10]. However, most literature on the subject deals with non-bulk structures [11]. For instance, Noronha et al. [12] investigated the geometrical accuracy of the holes in Ti64 lattice structures, observing that channels with a diameter of 400 µm or less are occluded by the powder.

Titanium alloys are a class of materials greatly appreciated in the aviation, chemical and biomedical fields. This is mainly related to their high specific strength [13], chemical resistance [14] and biocompatibility [15]. The application of AM technologies to process titanium alloys is very promising, due to the high costs and materials wastes associated with the conventional manufacturing techniques. Moreover, the typical industries that deploy these materials are usually characterized by small-lot productions and intricate designs [16]. Ti–6Al–4V (Ti64) is an α + β alloy, that shares the vast majority of the titanium market. However, most recently researchers began to focus their attention on alternative titanium alloys, more suitable for specific applications that require superior properties with respect to Ti64. One of these is the α + β (or near-β) alloy Ti–6Al–2Sn–4Zr–6Mo (Ti6246), characterized by interesting mechanical properties and higher maximum temperatures of application. Recently, Carrozza et al. [17] demonstrated the suitability and versatility of LPBF processes to manufacture this material. In fact, very promising combinations of mechanical properties were achieved via proper post-processing heat treatments. Peng et al. [18] demonstrated that exceptional hardness values can be achieved via short one-step heat treatments in the LPBF-processed material, further confirming the recent interest towards this material for AM applications [19]. Moreover, Ti6246 is characterized by a very ductile behavior in the as-built state, unlike Ti64 [20]. This feature might possibly result in easier handling of the parts and possibly improved processability.

Most of the works available in the literature focused on the assessment of the manufacturability limit of complex geometrical features via optimization of the design and/or process (e.g., support addition, scanning strategy variation). In this work a different approach was considered instead: two titanium alloys (Ti64 and Ti6246) were processed using the optimized combination of machine parameters for bulk parts, in order to manufacture specimens characterized by low thicknesses and small hollow horizontal channels. The final goal was to determine whether one of the two alloy is more suitable to manufacture intricate parts. In this study, process parameters optimized for thin parts production were not considered. In fact, the analyses conducted were aimed at investigating the processability of critical features of complex parts, made of bulk areas and thin/intricate parts simultaneously. In this framework, the adoption of a single combination of process parameters is mandatory. The comparative analysis presented in this work has a material-driven approach to the topic. The specimens were analyzed in terms of geometrical compliance, porosity, microstructure and hardness. Great attention was given to the process-generated defects, by deploying in-depth characterization techniques.

## 2 Materials and methods

### 2.1 Manufacturing Process

Spherical argon-atomized Ti64 and Ti6246 extra low interstitials (ELI) powders, supplied by TLS Technik GmbH, were used as feedstock material to manufacture the specimens investigated in this work. These two powders had similar particle sizes and low porosities (see Table 1; Fig. 1). The relative chemical composition is reported in Table 2.

**Table 1** Geometrical descriptors and porosities of the powders

| Alloy | $D_{10}$ (µm) | $D_{50}$ (µm) | $D_{90}$ (µm) | Powder porosity (%) |
|---|---|---|---|---|
| Ti64 | 25.9 | 39.5 | 56.1 | 0.19 |
| Ti6246 | 24.1 | 38.0 | 54.7 | 0.22 |

Bulk and tap densities were evaluated according to ASTM B527. The Hausner ratio and Carr Index were also calculated to compare the flowing/packing behavior of the two powders [21], as reported in Table 3.

Both powders were processed using a LPBF EOS M270 Xtended machine equipped with a Yb-fiber laser, characterized by a spot size of 100 µm and a maximum power of 200 W. A different set of optimized parameters was adopted

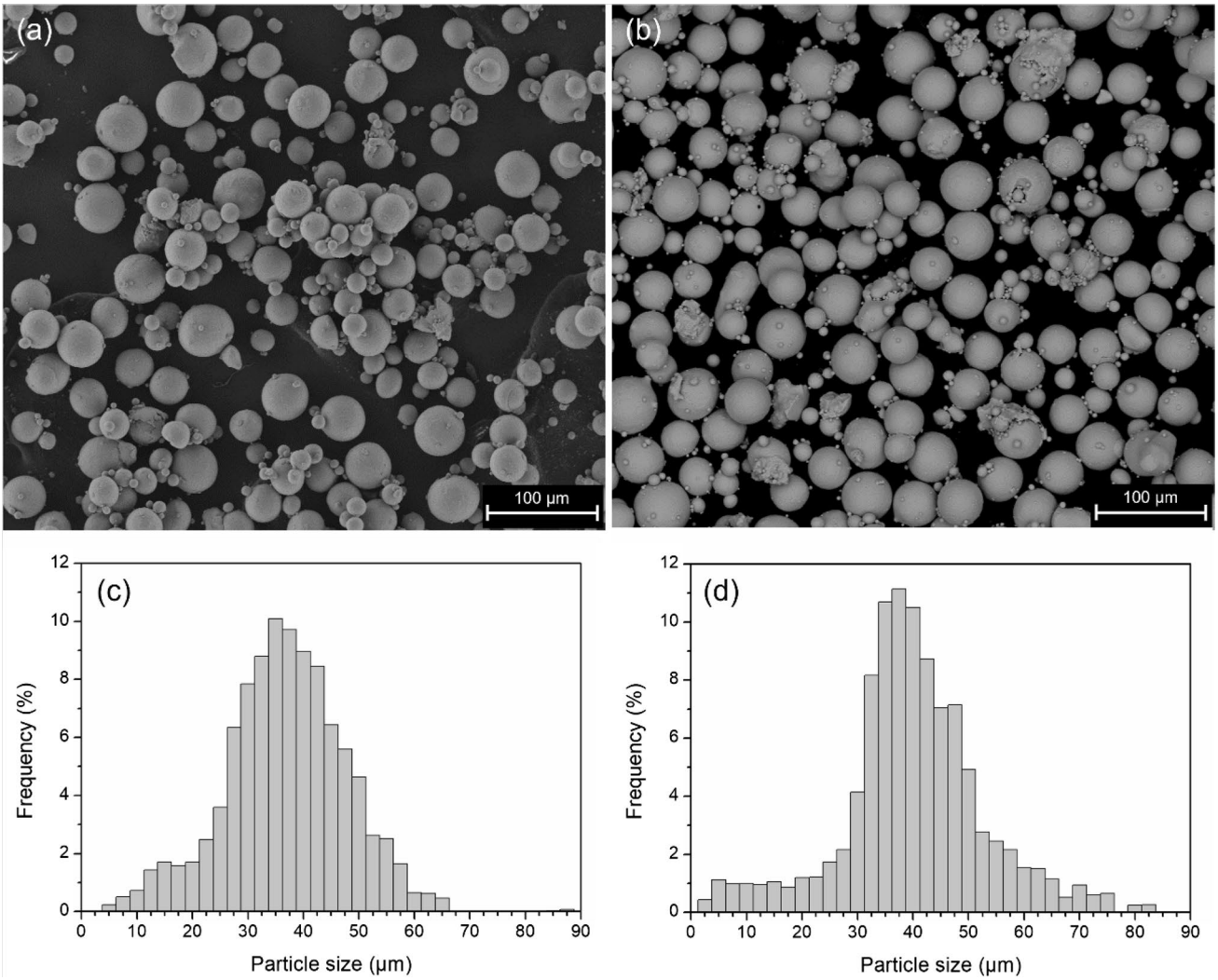


**Fig. 1** Representative scanning electron microscope images of the Ti64 (**a**) and Ti6246 (**b**) powders. Particle size distribution curves of the Ti64 (**c**) and Ti6246 (**d**) powders

**Table 2** Chemical compositions of the powders, as measured by the supplier

| Alloy | Composition (wt%) | | | | | | | | | | | |
|---|---|---|---|---|---|---|---|---|---|---|---|---|
| | Ti | N | C | H | Fe | O | Al | V | Mo | Zr | Sn | Other |
| Ti64 | Bal. | 0.003 | 0.01 | 0.002 | 0.183 | 0.083 | 5.86 | 3.99 | – | – | – | – |
| Ti6246 | Bal. | 0.005 | 0.01 | 0.002 | 0.031 | 0.118 | 5.96 | – | 5.89 | 3.67 | 1.85 | < 0.3 |

**Table 3** Rheological parameters of the feedstock powders

| Alloy | Bulk density (g/cm$^3$) | Tap density (g/cm$^3$) | Hausner ratio | Carr index | Flowing behavior |
|---|---|---|---|---|---|
| Ti64 | 2.24 ± 0.01 | 2.61 ± 0.01 | 1.16 ± 0.01 | 14.18 ± 0.80 | Good |
| Ti6246 | 2.27 ± 0.02 | 2.67 ± 0.01 | 1.18 ± 0.01 | 15.57 ± 1.09 | Good |

for each alloy, as reported in Table 4. The downskin and contour parameters cannot be disclosed due to a non-disclosure agreement with the producer of the machine. Nevertheless, these were kept the same for both materials, so that the comparative analysis would be consistent.

Two different groups of samples per material were manufactured with the aim to evaluate separately the effect of the wall thickness and the presence of horizontal channels. The former group consisted of six 10 mm × 13 mm thin wall specimens, characterized by progressively increasing thickness values, ranging from 0.3 to 5 mm, as schematized in Fig. 2. Additionally, a 10 mm × 13 mm × 5 mm "hollow channels" specimen was built. This was characterized by 3 vertically aligned through holes of 1, 2 and 3 mm in diameter, respectively. Each group of specimens per alloy was produced twice to provide statistically more relevant results.

## 2.2 Metallographic Analyses

All the specimens were cut along the building direction, mounted in conductive resin, ground using progressively finer SiC papers (up to 2400 grit) and then polished using a synthetic cloth paper and a suspension of colloidal $SiO_2$, water and $H_2O_2$. Microstructural assessments were conducted after chemically etching the specimens with a Kroll solution (93% $H_2O$, 5% $HNO_3$, 2% HF). The specimens were observed by means of optical microscope (OM) and scanning electron microscope (SEM) imaging. The instruments adopted were a Leica DMI 5000 M OM and a Phenom-XL SEM.

The average porosity was assessed by processing at least 20 optical micrographs (200x magnification) per specimen with the software ImageJ. A relatively high magnification and number of images were used in order to provide a high degree of representativity. Moreover, this methodology allowed a precise quantification of the pores < 5 µm. In general, a less time-consuming approach can be adopted by using lower magnifications, as performed by Karimi et al. [22]

A similar methodology was adopted to assess the dimensional compliance of the thin wall specimens with the original 3D design. The width of the samples was measured by crossing the cross-sectioned material with a grid of horizontal lines. A similar methodology was already successfully applied by Wu et al. [3].

Phase identification was performed by means of X-ray diffractometry (XRD), using a PANalytical X-Pert Philips diffractometer in a Bragg–Brentano configuration. The instrument deployed a Cu $K_\alpha$ radiation and operated at 40 kV and 40 mA. A step size of 0.013° and a 2θ range of 30–100° were considered.

Hardness was assessed via Vickers microhardness analyses, using a Leica VMHT hardness tester set to work with a load of 300 g applied for 15 s. A number of indentations ranging from 10 to 50 were performed on each specimen, depending on its size.

**Table 4** Process parameters adopted to process the Ti64 and Ti6246 alloys

| Alloy | Laser Power (W) | Scanning speed (mm/s) | Hatching distance (mm) | Platform temperature (°C) | Layer thickness (µm) | Scanning strategy |
|---|---|---|---|---|---|---|
| Ti64 | 170 | 1250 | 0.1 | 100 | 30 | Standard 67° EOS strategy |
| Ti6246 | 190 | 1250 | 0.1 | 100 | 30 | Standard 67° EOS strategy |

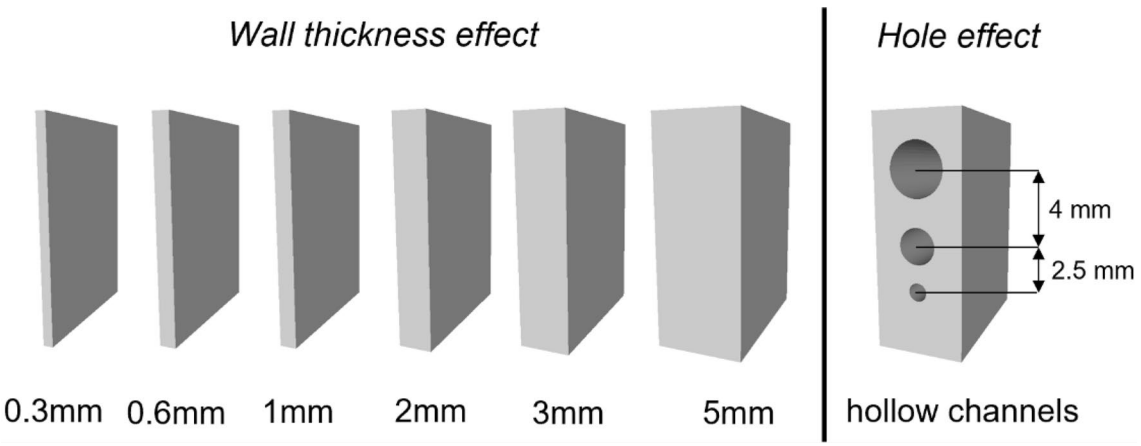


**Fig. 2** 3D designs of the specimens and relative nomenclature

### 2.3 X-ray Computed Tomography

Micro computed tomography (microCT) analyses were performed on the hollow channels specimens in order to further assess the geometrical compliance with the initial 3D design and the spatial distribution of the pores. The samples were inspected on a custom-developed X-ray microCT system consisting of a micro-focus X-ray tube (XWT-190-TCNF, X-RAY WorX), a 4000 × 4000 $px^2$ digital X-ray detector (XRD 1611 CP3, Perkin Elmer), and air-bearing motion axes. Further details on the system are available elsewhere [23]. The X-ray tube was operated at a voltage of 180 kV and 10 W target power using a 0.2 mm copper filter to harden the spectrum. 5001 projections with an integration time of 5.0 s each were recorded on a helical trajectory (500° scan angle, 19 mm pitch). Projection data were corrected for beam hardening and reconstructed into a volume consisting of 1750 × 1700 × 1950 voxel with a voxel size of 7.1 µm using Siemens CERA 5.1. Data analyses were performed in VG Studio MAX 3.4 (Volume Graphics). To assess the geometrical compliance with the original 3D design, the outer surface of the CT data was segmented using a gradient based surface determination and registered to the CAD model using a best fit algorithm. Subsequently, the deviations between the CT data and the CAD model were assessed by a nominal-actual comparison. For porosity analysis, volume data were filtered with a 3 × 3 × 3 median filter. Subsequently, porosity analyses were performed using the VGEasyPore module with sub-voxel accuracy, a relative threshold of 50% and a local area size of 10 voxel (diameter of the search area around each voxel to determine the local contrast). To render the analysis less prone to noise, defects were omitted if either the probability threshold (a non-disclosed quality metric) was below 0.1% or the defect size below 8 voxels. Pore parameters, such as position and equivalent diameter were exported for further analysis.

## 3 Results and Discussion

### 3.1 Effect of the Wall Thickness

The geometrical compliance with the original 3D design was evaluated in all the thin wall specimens via width measurements, as illustrated in Fig. 3. Overall, most of the specimens provided a slightly lower thickness with respect to the nominal values (up to 17% less). The only notable exception lied in the Ti64 0.3 mm specimen, that presented in-process delamination of the lower layers, resulting in a significant enlargement of the lower portion of the thin wall (Fig. 3a), and consequent growth of the relative error bar. This is a very common issues when processing titanium alloys via LPBF, mainly due to the high amount of residual stress that accumulates in the material. Machirori et al. [24] simulated the spatiotemporal evolution of temperature during the process to estimate the localization of the defects generated. The authors assessed that the bottom region is usually characterized by intense tensile stresses, possibly resulting in the delamination of the specimens in extreme conditions. In the specific case presented in this work, the possible cause for the geometrical degradation of the Ti64 0.3 mm specimens might have been caused by the high concentration of internal stress in a very confined volume, due to the reduced wall thickness. In general, the geometrical accuracy is somewhat dependent on the particle size distribution of the feedstock powder in LPBF-processed alloys [25]. Hence, the differences between the average widths and their nominal values were compared to the $D_{10}$, $D_{50}$ and $D_{90}$ values of the

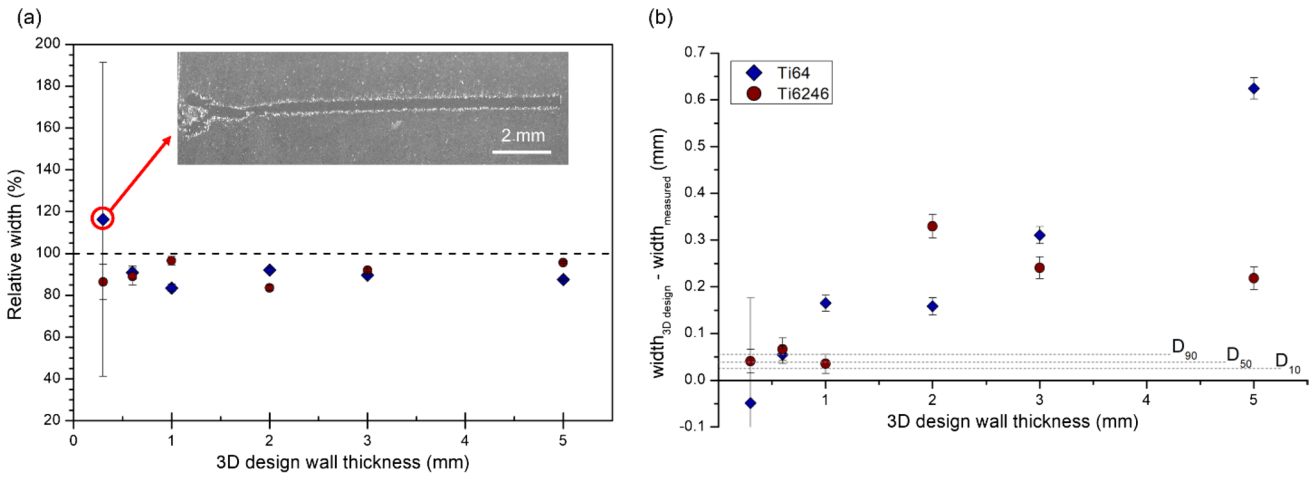


**Fig. 3** Relative geometrical compliance with the original 3D design (**a**) and width difference with the nominal values (**b**) in the thin wall specimens. The $D_{10}$, $D_{50}$ and $D_{90}$ reported were averaged between those of the Ti64 and Ti6246 alloy, since their values were very close

powders used during the process, as illustrated in Fig. 3b. It is evident that the dimensional variation from the 3D design increases with the nominal width of the thin wall specimen. The values achieved were significantly greater than the particle size for most specimens. Additionally, the feedstock powders showed very similar flowing behaviors. Therefore, the influence of the powder can be considered secondary in this evaluation.

One of the most common process-related defects in LPBF-processed materials is porosity. Pore formation is particularly critical in thin sections, due to the unique thermal phenomena and cooling paths that occur with respect to bulk parts. Moreover, conventionally small pore sizes ($\simeq$ 10 µm) might be critical in thin specimens, due to the void being a significant portion of the width of the sample. Hence, the average porosity was evaluated in all the thin walls and reported according to the thickness of the specimens, as provided in Fig. 4. Overall, an increase in porosity was detected in correspondence of the thinner samples for both alloys. Furthermore, the Ti64 alloy showed significantly lower relative densities (97%−99%) for the smaller samples. Acceptable values were achieved for a thickness of 3 mm or more. This result in in good agreement with the consideration made by Wu et al. [3], who stated that higher porosity values can be expected in thin Ti64 structures. In fact, the melt pool shape is very different and hard to predict in this context, thus resulting in a possible higher insurgence of process-related defects. Conversely, the Ti6246 alloy proved to be significantly less porous, achieving in the worst case a value < 0.2%. It is also worth mentioning that the maximum porosity detected in the Ti6246 samples (0.3 mm) overlapped with the minimum one in the Ti64 samples (3 mm). Since both the sets of parameters adopted to process the two materials can be considered as optimized, the lowest porosity achieved by the Ti6246 alloy might be due to its different alloying elements, hence composition. It is worth mention that the gas inclusions than enrich the molten material during LPBF processing can originate from pre-existing pores in the powder or directly being engulfed by the atmosphere of the process chamber. Nevertheless, no preferential gas entrapment was expected by neither of the two alloys, due to the same machine being used and the powder porosity values being very similar (Table 1).

The different porosity values might be related to the different solidification behavior of the two alloys. The melting range for the Ti6246 alloy is approximately 80 °C, whilst it accounts approximately 50 °C for Ti64 [26]. In general, a narrow melting range indicates a shorter solidification time. This affirmation is supported by the results obtained by Yu et al. [27] on laser-processed Ti–Zr congruent alloys, characterized by a very small solidification range, well comparable with other conventional Ti alloys (e.g., Ti64). In alloys with a short melting range, the gas bubbles in the molten material can hardly escape. This concept was validated in wire arc additive manufacturing processes by Hauser et al. [28], who found that very short solidification times can result in an increase of the retained porosity, due to the engulfed bubbles not being able to be released faster than the solidification front propagation. Nonetheless, this approach can be also used to evaluate the phenomena occurring in LPBF-processed titanium alloys.

In general, a wider solidification range is detrimental in terms of laser processing, due to the possible insurgence of solidification cracks, derived from a residual liquid film in correspondence of the grain boundaries. This is a well-known phenomenon in Al alloys [29]. However, this effect was not encountered in this case.

The correlation between a wider solidification range and a lower solidification time is acceptable if the difference in terms of cooling rates developed during the process can be considered comparable. In fact, the two alloys were processed using slightly differing laser powers (Table 4).

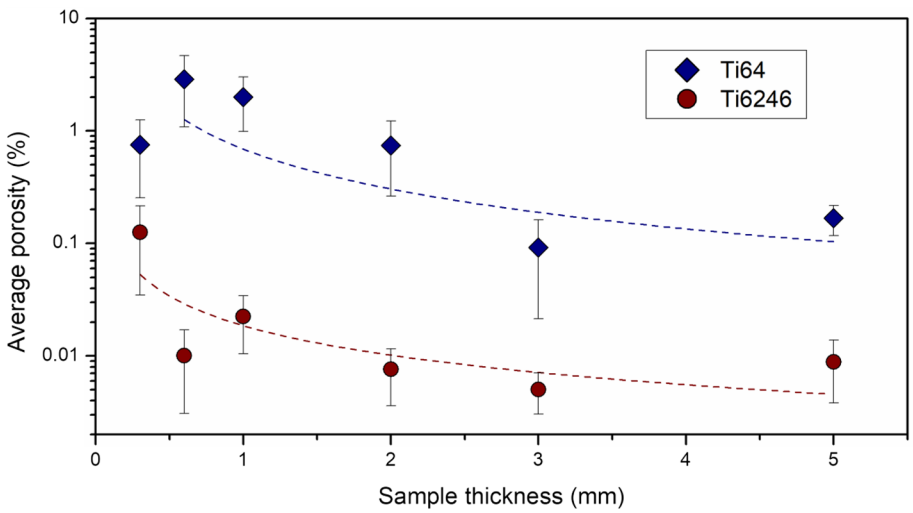


**Fig. 4** Porosity trends of the Ti64 and Ti6246 thin wall specimens

Notwithstanding that, such a small difference was considered negligible due to the relatively small dependence of the cooling rate with respect to small laser powder variations (≃ 10%). This is supported by the findings obtained by Calta et al. [30], which estimated the correlation between laser power and cooling rate in LPBF-processed titanium alloys via in situ high speed X-ray imaging.

In terms of pore morphology, representative micrographs are reported in Fig. 5. In general, most of the pores in all the specimens were rather spherical and relatable to entrapped gas. The number of defects with an irregular shape (e.g., lack of fusion) (as in Fig. 5a) was very low. No preferential accumulation of the defects in a specific area was detected in any sample.

A further assessment of the process-related defects was performed by evaluating the equivalent diameter of the pores in each condition and comparing their relative volumetric distributions (Fig. 6). For brevity purposes, only three specimens per alloy were considered (0.3 mm, 1 and 5 mm). These were chosen in order to represent low, intermediate and high wall thickness values.

In general, the Ti64 specimens provided a significant decrease in terms of pore $D_{50}$ with increasing wall thickness. This value went from approximately 20 µm in the 0.3 mm specimens to 3.5 µm in the 5 mm specimens. Conversely, the Ti6246 samples had a low-varying pore $D_{50}$, ranging between 5 and 7 µm. In both the alloys a certain increase in the maximum pore size detected was recorded for larger specimens, probably due to the coalescence of smaller gas bubbles. The low pore size measured allows to exclude the influence of spattering phenomena [31].

When two different alloys are compared, the effect of the different alloying elements must be taken into consideration. In fact, very high temperatures are achieved during LPBF processes. This phenomenon might lead to selective dealloying of some elements. This is a very well-known phenomenon in Al alloys [32]. The elements more prone to undergo selective evaporation are characterized by a high vapor pressure. The evolution of this parameter for a wide temperature range was investigated for the main elements found in the Ti64 and Ti6246 alloys (Ti, Al, V, Sn, Zr, Mo) (Fig. 7). The most critical (volatile) elements are Al and Sn. The former is contained in both alloys in the same amount, whilst the latter appears exclusively in Ti6246. Consequently, even if selective dealloying phenomena took place during LPBF processing, these were not a key factor in determining the final porosity of the material. In fact, the Ti6246 alloy would be more susceptible than Ti64 to the evaporation of alloying elements. Nevertheless, the Ti6246 alloy provided significantly lower porosity values.

The microstructures of the Ti64 and Ti6246 specimens are illustrated in Figs. 8 and 9a and b. The typical columnar prior-β grains were detected in both alloys (Fig. 8). This feature is the result of the epitaxial growth of the high temperature β grains, occurring during solidification due to the very directional cooling nature of the LPBF process. Needle-like laths were detected in both materials (Fig. 9a,b). These were assessed to be α' and α" martensite via XRD (Fig. 9c) in the Ti64 and Ti6246 samples,

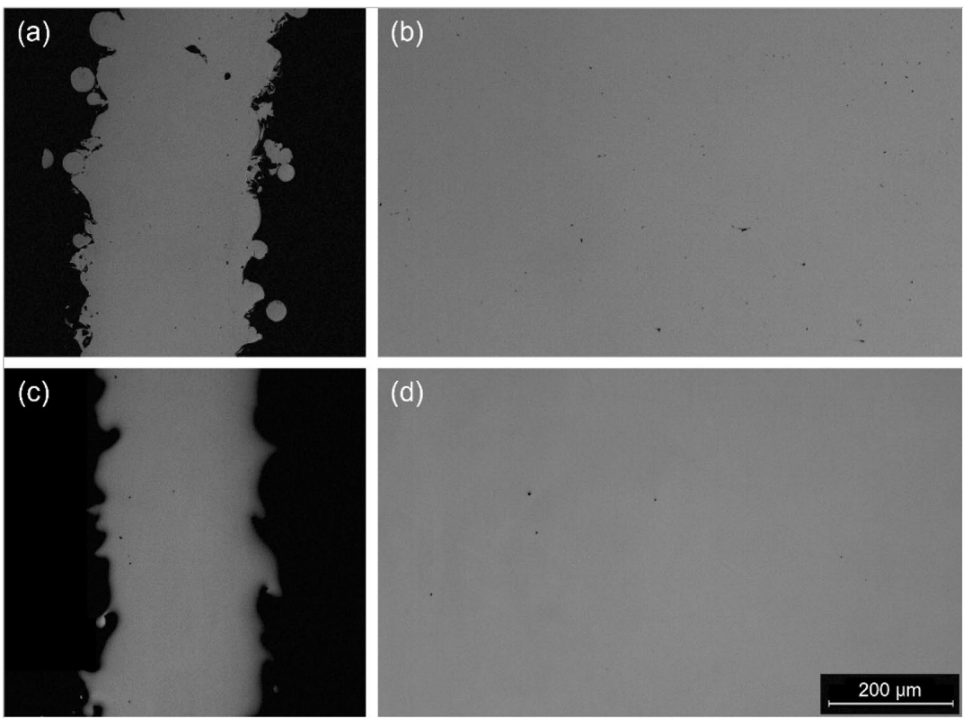


**Fig. 5** Representative micrographs of the pores found in the Ti64 0.3 mm (**a**), Ti64 5 mm (**b**), Ti6246 0.3 mm (**c**) and Ti6246 5 mm (**d**) specimens

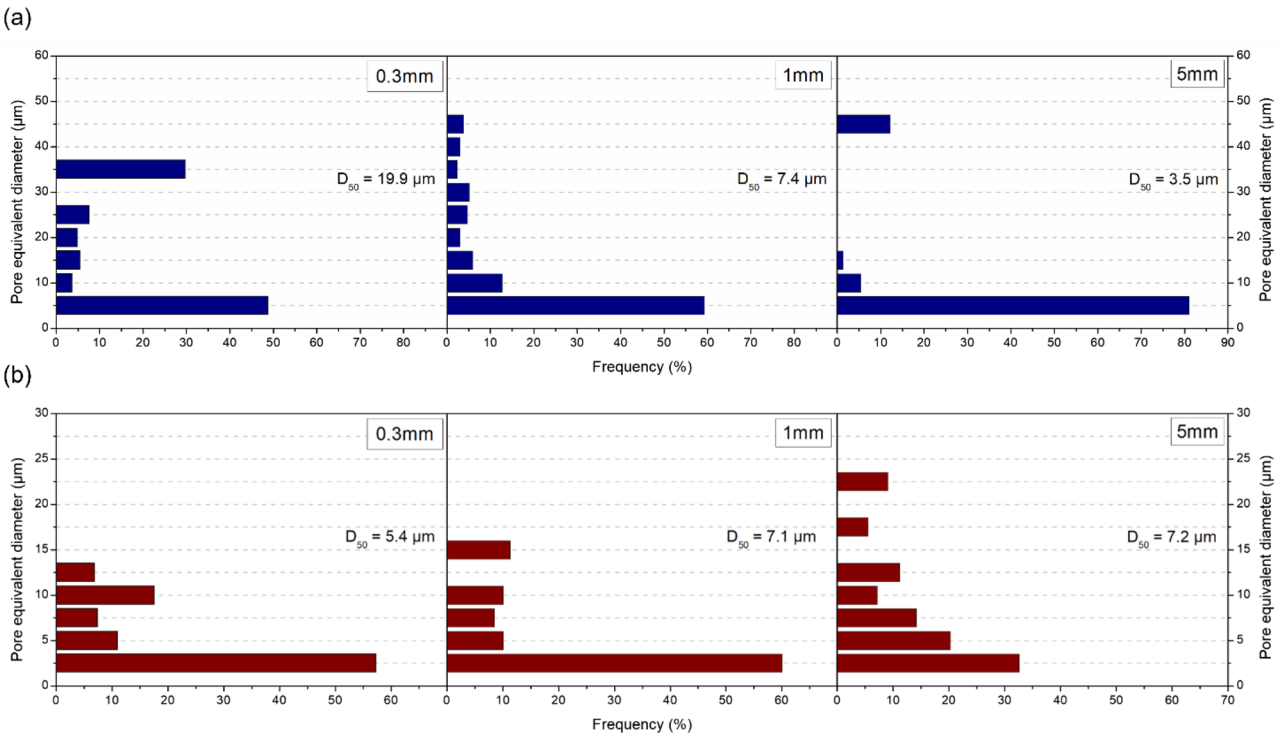


**Fig. 6** Pore equivalent diameter distribution for Ti64 (**a**) and Ti6246 (**b**) in low, intermediate, and high wall thickness specimens. Different scales and step sizes were adopted to improve readability

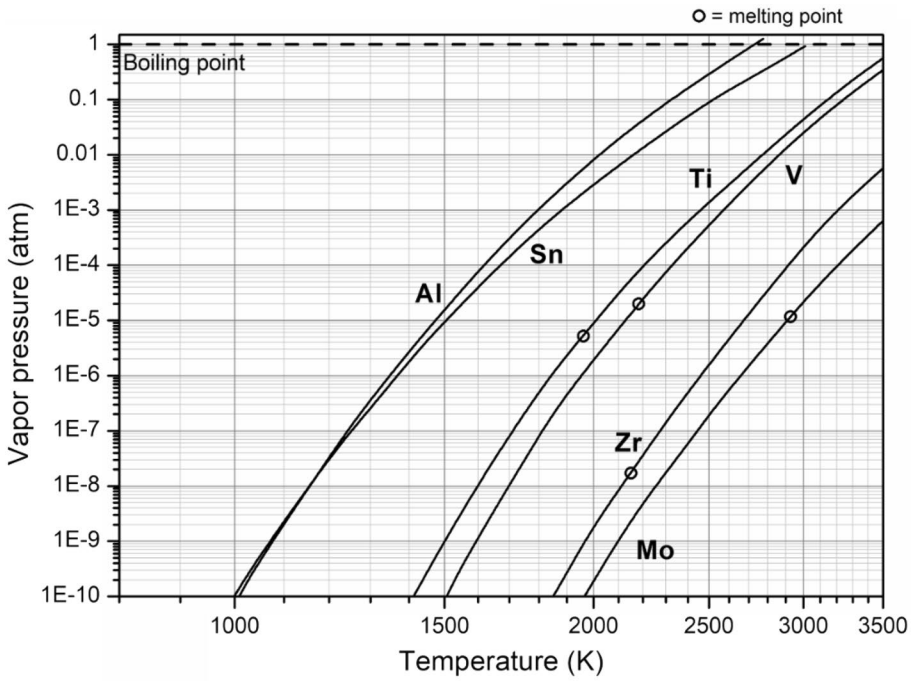


**Fig. 7** Vapor pressures of the main alloying elements in Ti64 and Ti6246 alloys (data obtained from [33])

respectively. The different type of martensite formed is dependent on the alloying elements in the two alloys, as described in a previous work from the authors [20].

Martensite width is a microstructural indicator than is frequently evaluated to assess the influence of the process on fast-cooled titanium alloys. Figure 10 shows the evolution

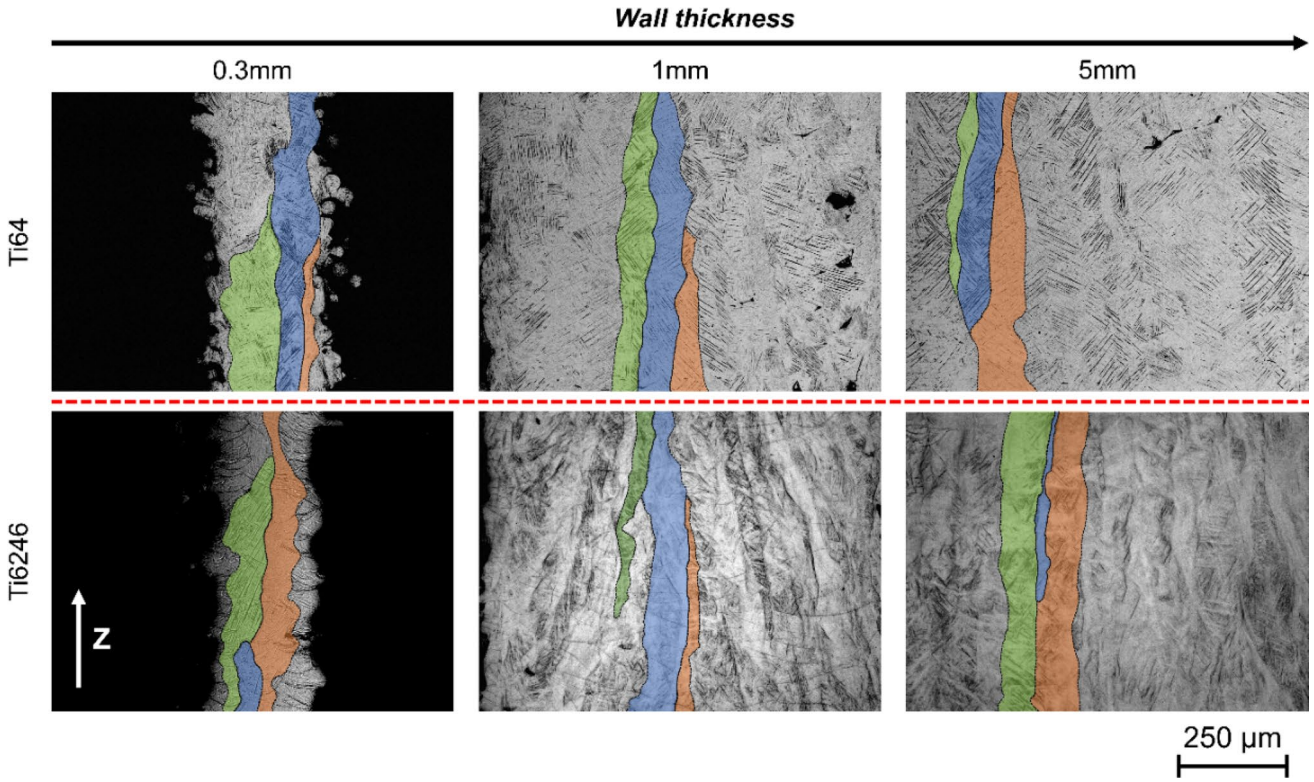


**Fig. 8** Optical micrographs with prior-β grains highlighted in low, intermediate and high wall thickness specimens

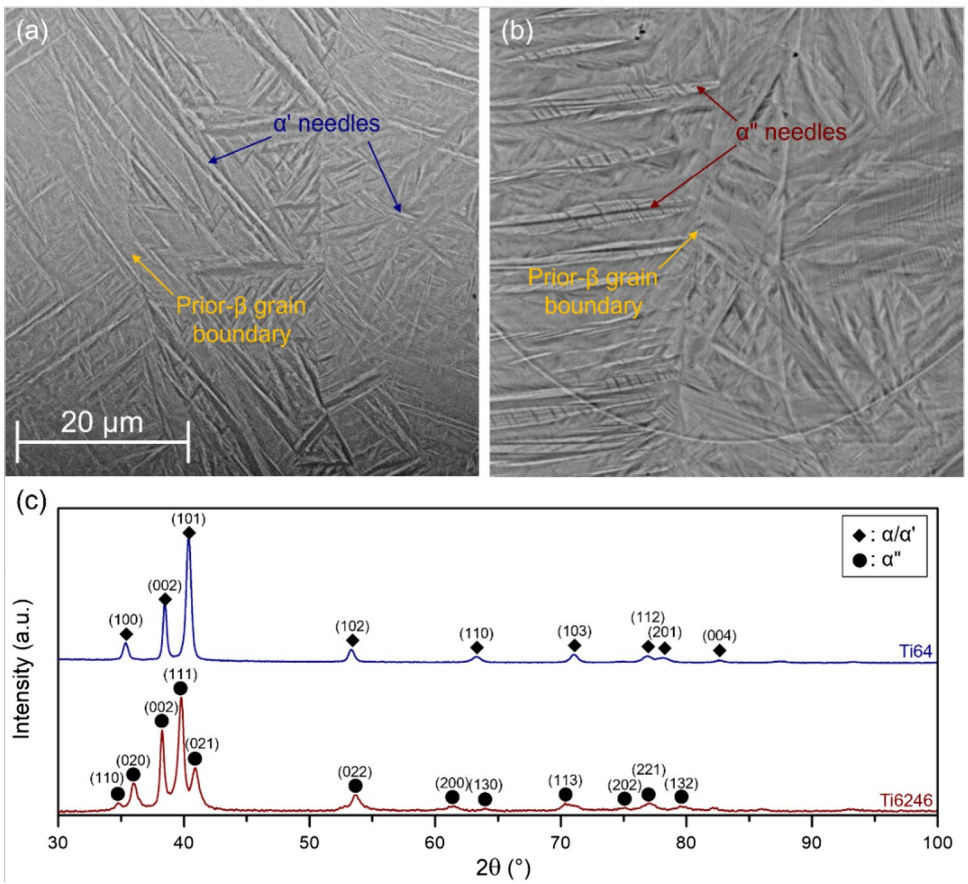


**Fig. 9** Representative SEM micrographs of the Ti64 (5 mm) (**a**) and Ti6246 (5 mm) (**b**) alloys. XRD spectra used for phase identification (**c**)

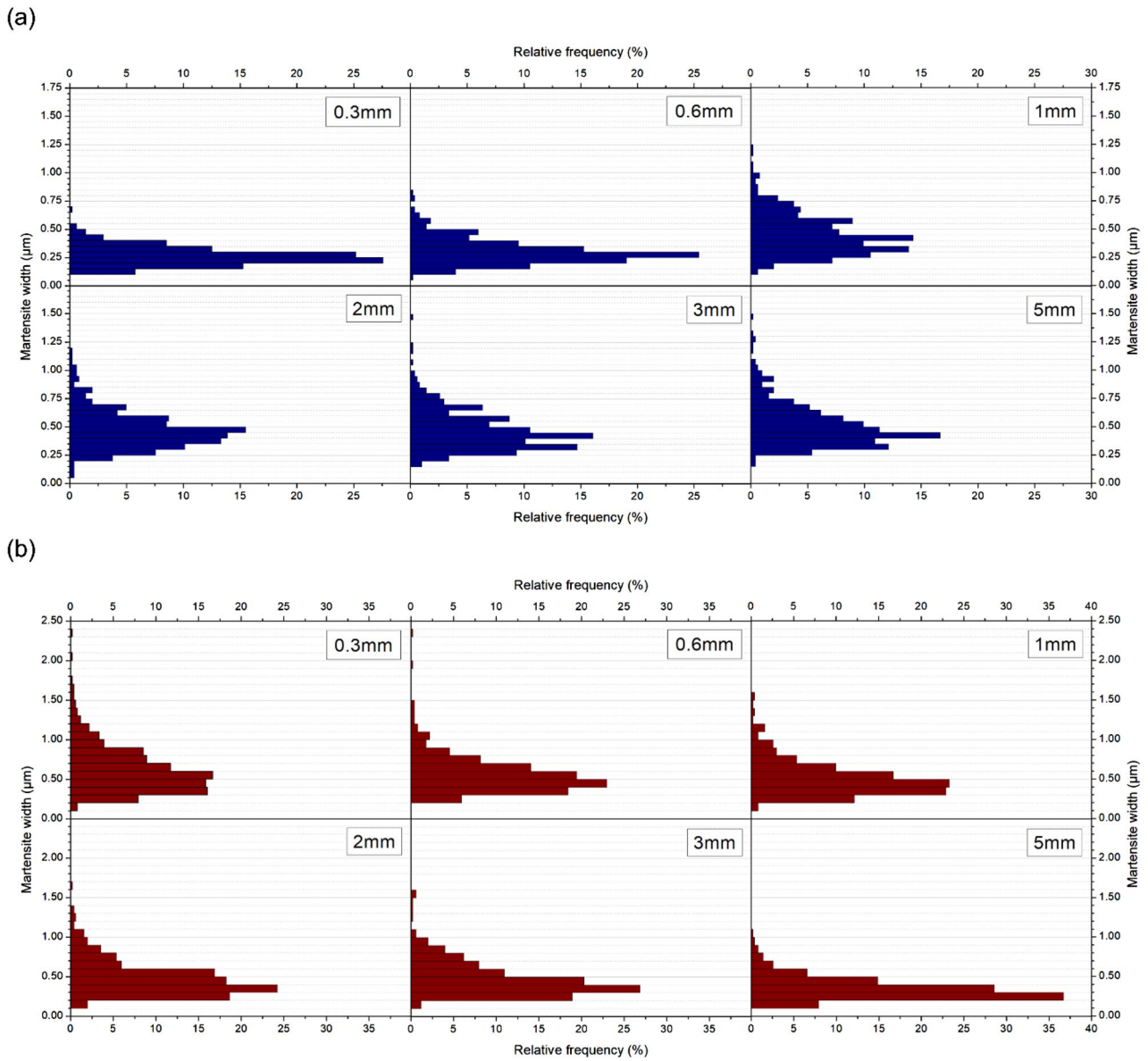


**Fig. 10** Martensite width distribution for the Ti64 (**a**) and Ti6246 (**b**) alloys. Different scales and step sizes were adopted to improve readability

of the martensite width in all the thin wall specimens. A progressive enlargement of the α' lath population, hence microstructural coarsening, is evident in the Ti64 samples (Fig. 10a). The values obtained are coherent with data from the literature [34]. Conversely, a narrowing distribution for increasing wall thickness, hence microstructural refining, was assessed in the Ti6246 samples (Fig. 10b). This result is corroborated by the evaluation of the mean values, presented in Fig. 11. It is clear that α' and α" are characterized by an opposite behavior with respect to the size of the specimens. In general, larger martensitic needles (α') can be found in samples that underwent higher cooling rates during solidification. This behavior is in good agreement with a work from Yang et al. [35], where the α' width of LPBF-processed Ti–6Al–4V samples was correlated to different process parameters (e.g., scanning strategy, speed). Conversely, Afonso et al. [36] reported that the size of the α" martensite in a Ti–Nb alloy for biomedical implants refines at higher cooling rates. Therefore, the results of this study seem to be in good agreement with the literature. Under this consideration, higher cooling rates can be assumed for the thicker specimens in this work. This is probably linked to the bigger amount of material surrounding a newly deposited track, thus resulting in more intense conductive cooling.

Hardness measurements were also carried out, as summarized in Fig. 12. The Ti64 specimens provided higher hardness with respect to the Ti6246 ones in all conditions considered. This is due to the different type of martensite in

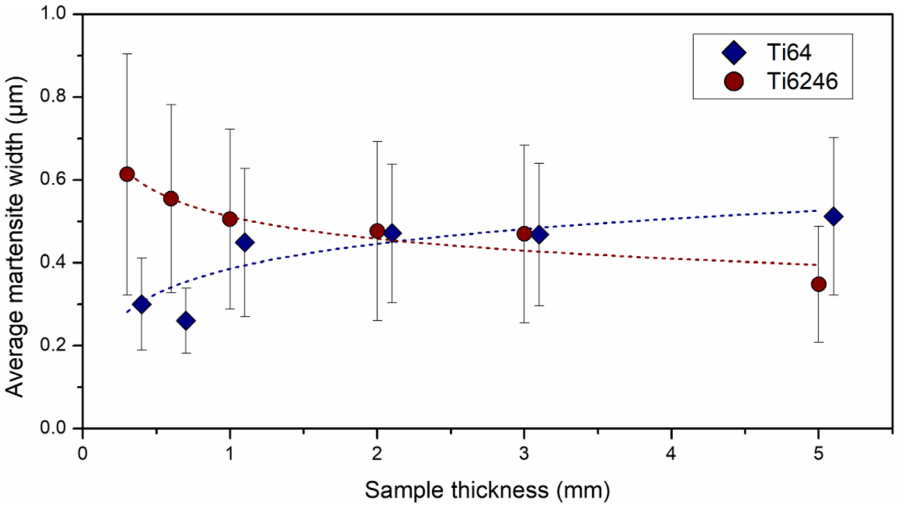


**Fig. 11** Martensite width trends of the Ti64 and Ti6246 thin wall specimens. The Ti64 values were slightly shifted to the right to improve readability

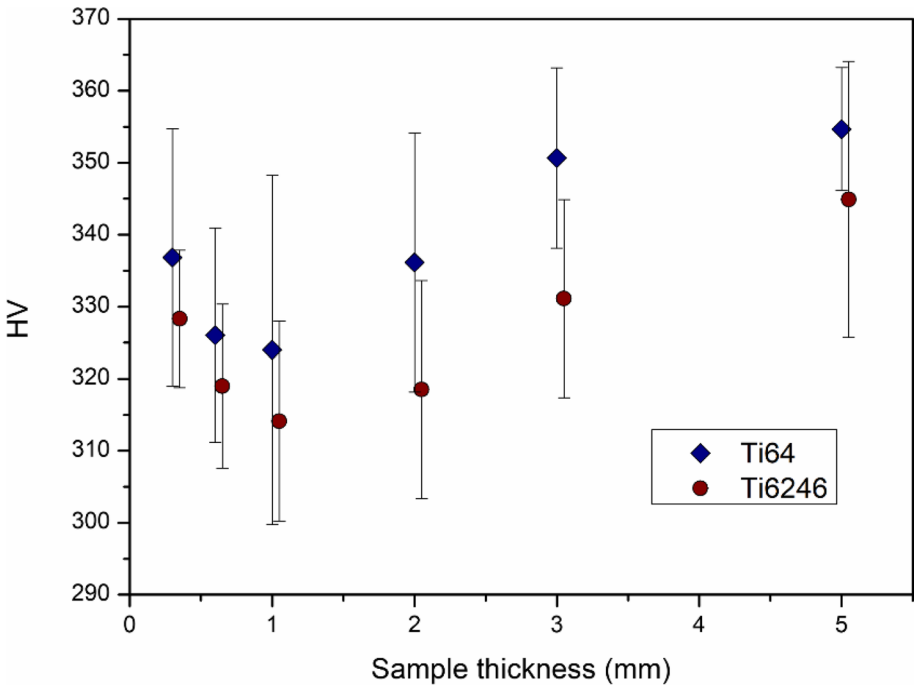


**Fig. 12** Vickers microhardness trends of the Ti64 and Ti6246 thin wall specimens. The Ti6246 values were slightly shifted to the right to improve readability

the two alloys. It is well-known that α' martensite (Ti64) is a moderate hardener and strengthener in titanium alloys [37]. Oppositely, α" martensite has a softening effect and usually results in a decrease in hardness [20].

The influence of the samples thickness on the hardness of the two alloys was similar, as in both scenarios an initial decrease was encountered up to reaching a minimum in the 1mm specimens. Then a progressive increase was measured for increasing thickness values. This effect is not directly relatable to the martensite width (Fig. 11). Probably other factors influenced the behavior of the specimens, such as internal stress accumulation and porosity. Width variations in the columnar prior-β grains might be another phenomenon influencing the hardness variations. The clear mechanism is still not completely understood. Nevertheless, the authors suggest a clear influence of multiple phenomena. It is possible that at lower sample thickness values (< 2mm) the predominant factor might be the variation in martensite size, providing a hardening effect for α', and vice versa for α".

### 3.2 Effect of the Hollow Channels

The geometrical compliance of the hollow channels specimens was investigated by means of microCT analyses and compared with the initial 3D design (Fig. 13). This is becoming a standard practice in order to reconstruct the volume of AM-processed specimens [38], particularly interesting when dealing with lattice structures [39]. For instance,

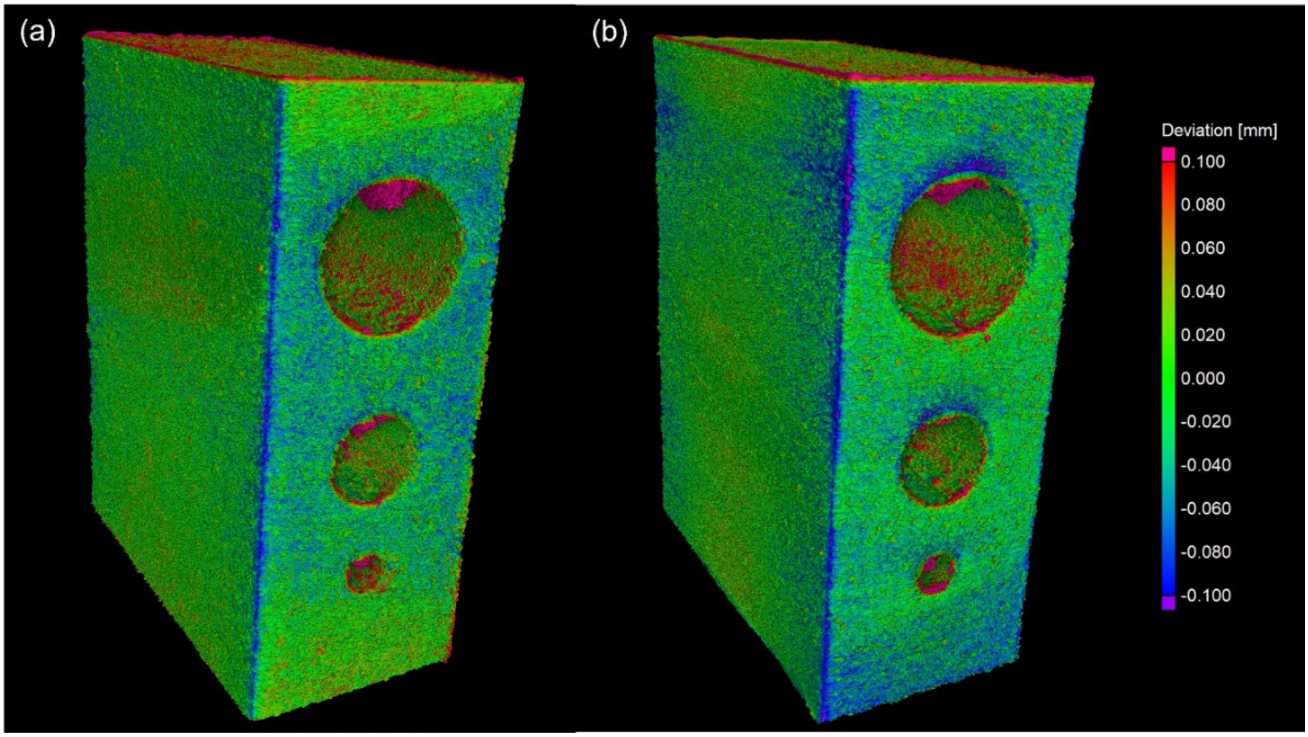


**Fig. 13** Geometrical compliance evaluation via microCT 3D reconstructions of the Ti64 and TI6246 hollow channels specimens

Vilardell et al. [40] adopted this technique to optimize the topology of Ti64 structures for biomedical applications. In this work, both the alloys considered provided a good fit with the original shape in the lateral sides. A negative variation was found in correspondence of the edges of the samples. Conversely, the upper surfaces were characterized by a deviation of up to + 100 µm, probably due to the roughness granted by the laser scanning lines. These results are in good agreement with the surface characterization performed by Cabrini et al. [15] on LPBF-produced Ti64 specimens via confocal imaging. In fact, the specimens analyzed in that work provided a variation of up to 80–100 µm, due to the visible marks left by the laser tracks.

The analysis of the hollow channels (Fig. 14a,b) proved to be more complex. Moreover, significantly higher deviations from the original design were found. The analysis of the deviation distribution curves (Fig. 14c) highlighted three main peaks of interests for both alloys. A first peak, corresponding to very negative deviations (I), corresponding to the lower surfaces (bases). This effect was linked to the mechanical removal of the specimens from the building platform, resulting in material loss. This is a necessary operation, thus its influence on the overall dimensional accuracy will not be discussed. A second peak of good compliance (II), varying from − 0.1 to a + 0.1 mm, corresponds to the lateral and upper surfaces, as evidenced before. A third peak (III), characterized by significant positive variations is related to the hollow channels, where the greatest differences from the original geometry were detected. In general, the lowest compliance was found in the upper parts of each channel, probably due to the lack of a local solid substrate to support the weight of the material. In fact, when the layer is melted, the newly generated solid metal is directly located on a portion of unmelted powder, which might locally collapse, resulting in the typical U-shaped regions clearly visible in Fig. 13. Another possible cause for the low geometrical accuracy of the through holes might be related to the presence of partially sintered powder and/or stress-induced deformation. These are well-known phenomena in overhanging and lattice structures' design [41].

Overall, the Ti64 alloy provided a slightly better dimensional accuracy inside the holes. In fact, the surface fraction > 0.6 mm was approximately 0.5%, whilst it accounted for 1.25% in the Ti6246 alloy. It is also worth mentioning that the lack of compliance appeared to be more critical in the smaller (1 mm) channels.

In terms of porosity, the microCT analysis was adopted to investigate the spatial arrangement of the macro-pores (> 20 µm) (Fig. 15). The micro-pores were not considered due to the resolution limits of the instrument. In fact, microCT techniques are better suited to investigate lack of fusion defects in AM-processed materials, as gas porosities are usually too small to be detected. Notwithstanding this

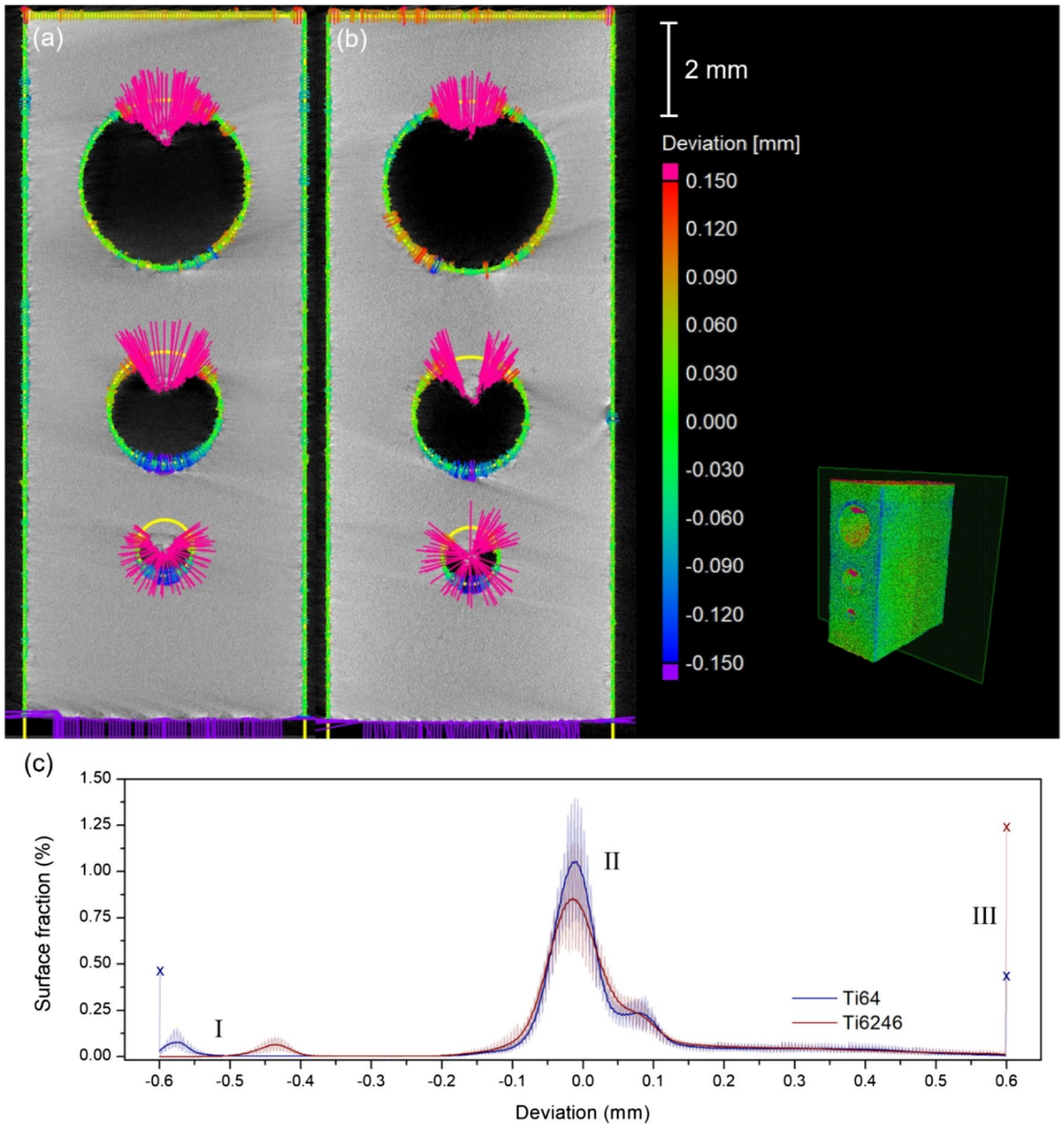


**Fig. 14** Representative 2D slices of the Ti64 (**a**) and Ti6246 (**b**) specimens obtained via microCT, the lengths of the deviation vectors are exaggerated for better visibility. Relative deviation distribution from the original 3D design (**c**)

limit, these types of measurements are very popular in AM research [42].

In this work, the maximum size detected was approximately 200 µm in both materials. Overall, the vast majority of such defects was found in correspondence of the hollow channels, as reported in Fig. 16, where each point represents a pore (detected via microCT), described according to its location along the Z axis and the relative equivalent diameter. By comparing the Z values where most of the bigger pores are accumulated with the design of the component (right part of Fig. 16), it is evident that most of the macro-pores were concentrated both on the upper and lower regions of the holes. In the former case, this is probably due to the lack of a solid substrate, as discussed before. Instead, the higher porosity found in the lower region was probably caused by the lack of remelting, given the presence of the channel directly above.

The majority of the macro-pores of both materials were located in the 20–50 µm size range (Fig. 17). The maximum size pores were found in the Ti6246 alloy. Nevertheless, the distribution of the pore equivalent diameters was more shifted towards lower values for this material, whilst the Ti64 alloy distribution appeared more evenly distributed towards a large range of sizes. Therefore, it seems that the

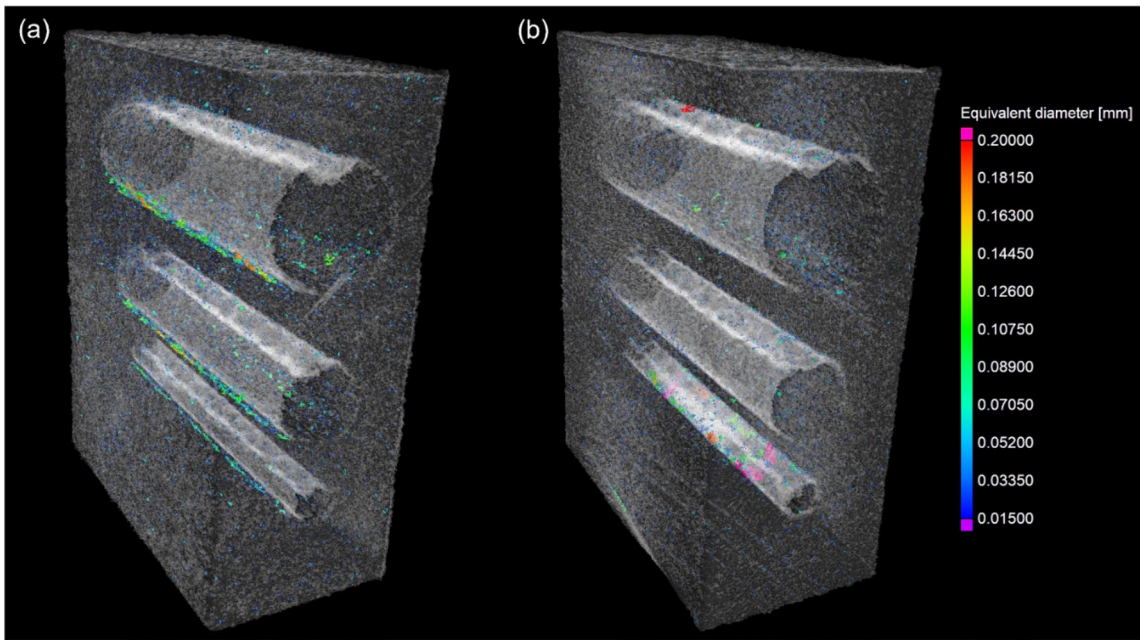


**Fig. 15** Porosity distribution in the Ti64 (**a**) an Ti6246 (**b**) hollow channels specimens

lack of fusion defects generated in the hollow channels are on average smaller in the Ti6246 alloy. Furthermore, the macro-porosity accounted for 0.036% and 0.028% in the Ti64 and Ti6246 specimens, respectively.

SEM observations of the hollow channels' areas (Fig. 18) seem to confirm the previous hypotheses. In fact, the macro-pores detected in correspondence of the lower half of the horizontal struts presented the typical irregular morphology, linked with the lack of appropriate remelting of the layer (Fig. 18a). This is typically recognizable by the lack of sphericity of these defects [43]. The analysis of the upper part of the channels evidenced the presence of equiaxed prior-β grains, instead of columnar, suggesting a lower and non-directional cooling rate (Fig. 18b), due to

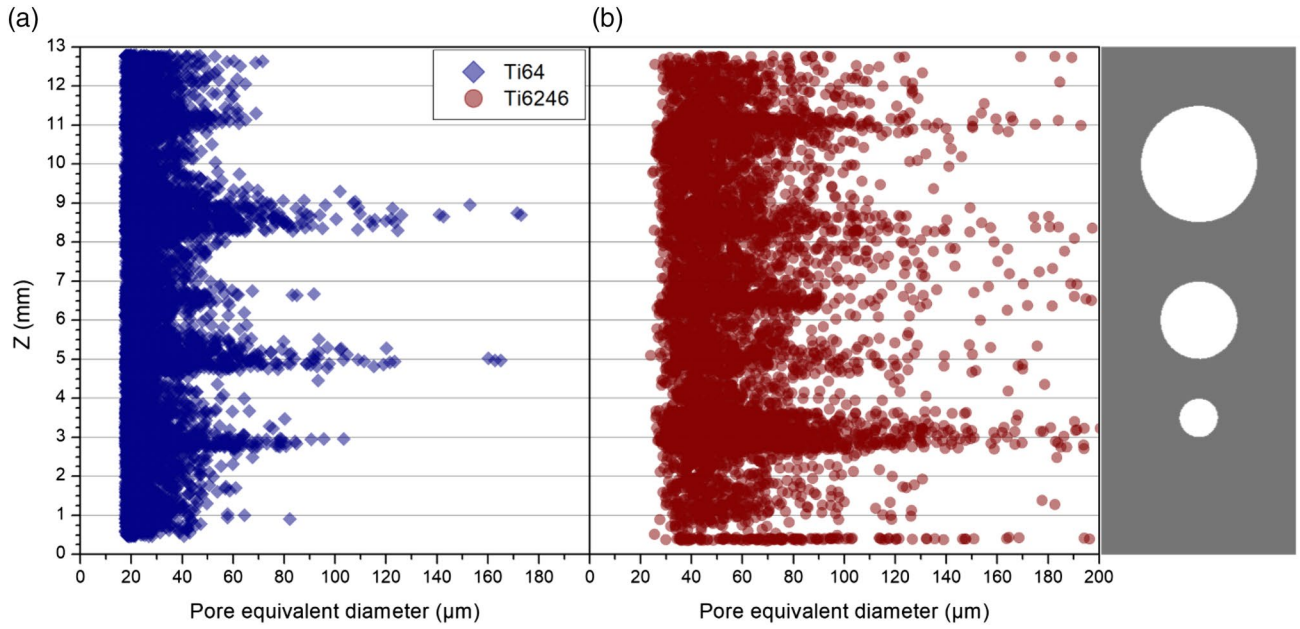


**Fig. 16** Macro-pores represented as a function of their location height (Z) and size in the Ti64 (**a**) and Ti6246 (**b**) hollow channels specimens. A representation of the design of the specimens in presented on the right for reference

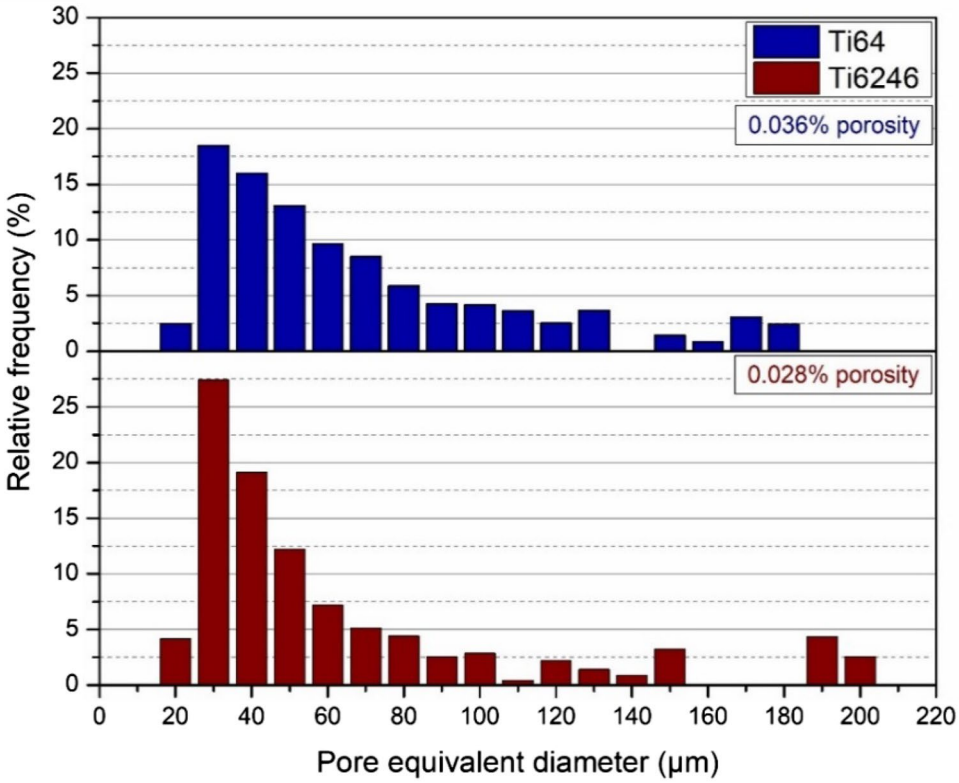


**Fig. 17** Pore size distributions obtained via microCT analyses

the lower thermal conductivity of the powder with respect to the bulk material. In fact, equiaxed prior-β grains do not form in standard conditions in LPBF-processed Ti64. This is the result of epitaxial growth, given by the very high directional cooling rates achieved, headed towards the baseplate, acting as a heat sink [44]. This very high solidification rate also induces massive martensite formation, as discussed before [45]. In this case, the directional component of cooling disappears, due to the powder having a significantly lower thermal conductivity with respect to the bulk material [46]. Therefore, solid state conduction occurs more homogeneously, from a directional point of view, leading to the formation of equiaxed grains. This surely results in a slightly lower cooling rate. Nevertheless, this is still high enough to provide martensite formation. Moreover, several unmelted particles were found (Fig. 18c). This phenomenon, caused by the powder engulfment due to the contact of the liquid metal with the

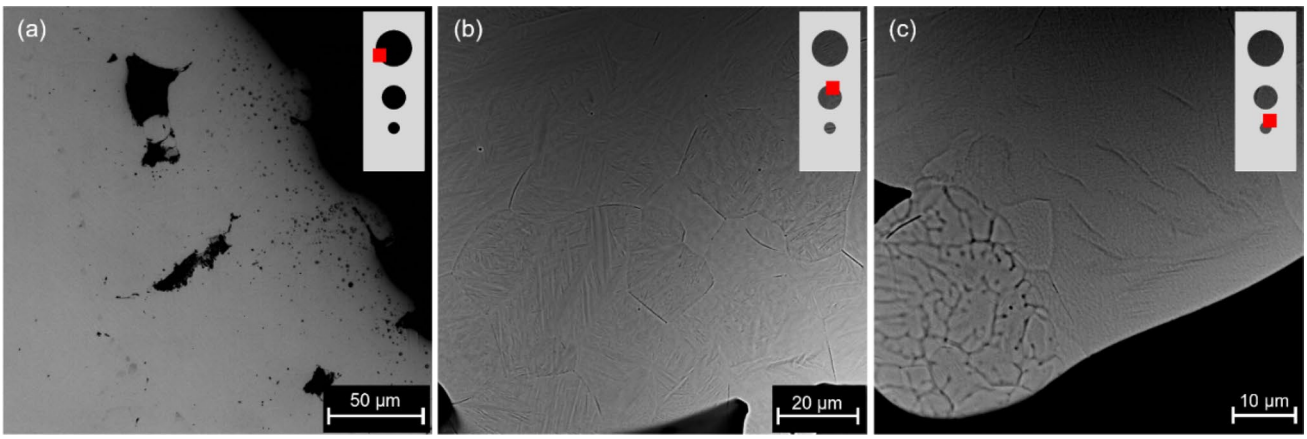


**Fig. 18** Representative SEM micrographs of the hollow channels specimens in both alloys, highlighting the different features observed: macro-defects in correspondence of the channels (**a**), equiaxed grains above the channels (**b**) and unmelted particles in the upper part of the channels (**c**). A schematic representation of the location of each micrograph is provided for each image

particles underneath, surely contributed to the exacerbation of the geometrical compliance of the specimens. This defect is commonly found in these types of structures, as reported by other authors [11, 47].

## 4 Conclusions

In this work, a well-established titanium alloy (Ti–6Al–4V) and a newly processed one (Ti–6Al–2Sn–4Zr–6Mo) were comparatively investigated with the aim of evaluating their behavior when dealing with critical-to-manufacture LPBF geometries, such as thin walls and hollow channels. Process parameter combinations optimized for bulk parts production were considered, so that this analysis can be extended to large parts with small features. This comparison is industrially relevant, due to both these alloys being applied in industrial fields – i.e., aerospace – where these complex geometries are fundamental. Additionally, the LPBF-processed Ti6246 alloy is rather new and no current record of its investigation in terms of manufacturability of complex geometries is available in the literature. The following main results were obtained:

- Both materials proved to be suited for fabrication at low wall thickness values, reaching values as low as 300 µm. In this case, the Ti6246 alloy had a good geometrical compliance with the original design, whilst the Ti64 alloy showed delamination phenomena occurring in correspondence of the lowest layers.
- Overall, porosity increased as the thickness of the specimens decreased. Furthermore, the Ti6246 alloy was always characterized by significantly lower porosity values with respect to Ti64. This last effect was correlated to the different solidification ranges.
- In terms of microstructure, both materials were characterized by the massive presence of α' or α" martensite in Ti64 and Ti6246 respectively, due to the different alloying elements. α' laths became increasingly larger as the thickness of the samples increase. Conversely, α" provided an opposite trend.
- The analysis of the specimens with horizontal hollow channels demonstrated that these geometrical features are critical for geometrical compliance, mainly due to the significant amount of rough surfaces and residual adhered powders developed in the inner part of the channels.
- In correspondence of the channels, a significant number of lack of fusion porosities was found in both materials. These defects appeared to be slightly more frequent in the Ti64 alloy. Their size was comparable in both alloys.

In general, the Ti6246 alloy appeared to be more suited for thin features fabrication in bulk components and porosity minimization, whilst the Ti64 alloy provided a superior geometrical compliance in the hollow channels.

**Acknowledgements** The authors would like to acknowledge the European research project MANUELA Additive Manufacturing using Metal Pilot Line (Project ID 820774) which received funding from the European Union's Horizon2020 research and innovation program. The authors would also like to express their appreciation to Dr. Emanuela Gallione and Dr. Alain Küng for their assistance.

**Funding** Open access funding provided by Università degli studi di Bergamo within the CRUI-CARE Agreement. This research was funded by Horizon 2020 research and innovation program with Grant Number 820774.



## References

1. V. Pandiyan, R. Drissi-Daoudi, S. Shevchik, G. Masinelli, T. Le-Quang, R. Logé, K. Wasmer, Deep transfer learning of additive manufacturing mechanisms across materials in metal-based laser powder bed fusion process. J. Mater. Process. Technol. **303**, 117531 (2022)
2. F. Calignano, G. Cattano, D. Manfredi, Manufacturing of thin wall structures in AlSi10Mg alloy by laser powder bed fusion through process parameters. J. Mater. Process. Technol. **255**, 773–783 (2018)
3. Z. Wu, S.P. Narra, A. Rollett, Exploring the fabrication limits of thin-wall structures in a laser powder bed fusion process. Int. J. Adv. Manuf. Technol. **110**, 191–207 (2020)
4. C. Chen, Z. Xiao, H. Zhu, X. Zeng, Deformation and control method of thin-walled part during laser powder bed fusion of Ti–6Al–4V alloy. Int. J. Adv. Manuf. Technol. **110**, 3467–3478 (2020)
5. A. Kushwaha, A.K. Subramaniyan, N.B. Kenchappa, S. Barad, Microstructure, mechanical, and wear properties of thin-walled Ti6Al4V parts produced using laser powder bed fusion technique. Mater. Lett. **308**, 131138 (2022)
6. M. Balbaa, R. Hussein, L. Hackel, M. Elbestawi, A novel post-processing approach towards improving hole accuracy and surface integrity in laser powder bed fusion of IN625. Int. J. Adv. Manuf. Technol. **119**, 6225–6234 (2022)
7. J. Kranz, D. Herzog, C. Emmelmann, Design guidelines for laser additive manufacturing of lightweight structures in TiAl6V4. J. Laser Appl. **27**, S14001 (2015)
8. T. Dahmen, C.G. Klingaa, S. Baier-Stegmaier, A. Lapina, D.B. Pedersen, J.H. Hattel, Characterization of channels made by laser

powder bed fusion and binder jetting using X-ray CT and image analysis. Addit. Manuf. **36**, 101445 (2020)
9. M. Baier, M. Sinico, A. Witvrouw, W. Dewulf, S. Carmignato, A novel tomographic characterisation approach for sag and dross defects in metal additively manufactured channels. Addit. Manuf. **39**, 101892 (2021)
10. F. Ceccanti, A. Giorgetti, G. Arcidiacono, P. Citti, Laser powder bed fusion: A review on the design constraints. IOP Conf. Ser. Mater. Sci. Eng. **1038**, 012065 (2021)
11. J. Noronha, M. Qian, M. Leary, E. Kyriakou, A. Almalki, S. Brudler, M. Brandt, Additive manufacturing of Ti–6Al–4V horizontal hollow struts with submillimetre wall thickness by laser powder bed fusion. Thin-Walled Struct. **179**, 109620 (2022)
12. J. Noronha, M. Leary, M. Qian, E. Kyriakou, M. Brandt, Geometrical parameters and mechanical properties of Ti6Al4V hollow-walled lattices. Mater. Sci. Eng. A **840**, 142667 (2022)
13. X. Yang, W. Ma, Z. Zhang, S. Liu, H. Tang, Ultra-high specific strength Ti6Al4V alloy lattice material manufactured via selective laser melting. Mater. Sci. Eng. A **840**, 142956 (2022)
14. L. Casanova, M. La Padula, M. Pedeferri, M.V. Diamanti, M. Ormellese, An insight into the evolution of corrosion resistant coatings on titanium during bipolar plasma electrolytic oxidation in sulfuric acid. Electrochim. Acta **379**, 138190 (2021)
15. M. Cabrini, A. Carrozza, S. Lorenzi, T. Pastore, C. Testa, D. Manfredi, P. Fino, F. Scenini, Influence of surface finishing and heat treatments on the corrosion resistance of LPBF-produced Ti–6Al–4V alloy for biomedical applications. J. Mater. Process. Technol. **308**, 117730 (2022)
16. D.-S. Shim, J.-Y. Seo, H.-S. Yoon, K.-Y. Lee, W.-J. Oh, Additive manufacturing of porous metals using laser melting of Ti6Al4V powder with a foaming agent. Mater. Res. Express **5**, 86518 (2018)
17. A. Carrozza, A. Aversa, P. Fino, M. Lombardi, Towards customized heat treatments and mechanical properties in the LPBF-processed Ti–6Al–2Sn–4Zr–6Mo alloy. Mater. Des. **215**, 110512 (2022)
18. H. Peng, S. Wu, W.H. Kan, S.C.V. Lim, Y. Zhu, A. Huang, Rapid hardening response of ultra-hard Ti–6Al–2Sn–4Zr–6Mo alloy produced by laser powder bed fusion. Scr. Mater. **226**, 115209 (2023)
19. W.H. Kan, H. Peng, S. Lim, Y. Zhu, K. Zhang, A. Huang, The mechanisms behind the tribological behavior of titanium alloys processed by laser powder bed fusion sliding against steel. Tribol. Int. **180**, 108279 (2023)
20. A. Carrozza, A. Aversa, P. Fino, M. Lombardi, A study on the microstructure and mechanical properties of the Ti–6Al–2Sn–4Zr–6Mo alloy produced via laser powder Bed Fusion. J. Alloys Compd. **870**, 159329 (2021)
21. S. Spath, H. Seitz, Influence of grain size and grain-size distribution on workability of granules with 3D printing. Int. J. Adv. Manuf. Technol. **70**, 135–144 (2014)
22. M.H.S. Karimi, M. Yeganeh, S.R.A. Zaree, M. Eskandari, Corrosion behavior of 316L stainless steel manufactured by laser powder bed fusion (L-PBF) in an alkaline solution. Opt. Laser Technol. **138**, 106918 (2021)
23. B.A. Bircher, F. Meli, A. Küng, R. Thalmann, METAS-CT: Metrological X-ray computed tomography at sub-micrometre precision, in *euspen's 20th International Conference & Exhibition*, Geneva, 8–12 June 2020
24. T. Machirori, F.Q. Liu, Q.Y. Yin, H.L. Wei, Spatiotemporal variations of residual stresses during multi-track and multi-layer deposition for laser powder bed fusion of Ti–6Al–4V. Comput. Mater. Sci. **195**, 110462 (2021)
25. S. Gruber, C. Grunert, M. Riede, E. López, A. Marquardt, F. Brueckner, C. Leyens, Comparison of dimensional accuracy and tolerances of powder bed based and nozzle based additive manufacturing processes. J. Laser Appl. **32**, 32016 (2020)
26. R. Boyer, E.W. Collings, G. Welsch (eds.), *Materials Properties Handbook: Titanium Alloys* (ASM International, Materials Park, 1994)
27. Q. Yu, C. Wang, D. Wang, X. Min, Microstructure and properties of Ti–Zr congruent alloy fabricated by laser additive manufacturing. J. Alloys Compd. **834**, 155087 (2020)
28. T. Hauser, R.T. Reisch, P.P. Breese, B.S. Lutz, M. Pantano, Y. Nalam, K. Bela, T. Kamps, J. Volpp, A.F.H. Kaplan, Porosity in wire arc additive manufacturing of aluminium alloys. Addit. Manuf. **41**, 101993 (2021)
29. H.E. Sabzi, S. Maeng, X. Liang, M. Simonelli, N.T. Aboulkhair, P.E.J. Rivera-Díaz-del-Castillo, Controlling crack formation and porosity in laser powder bed fusion: Alloy design and process optimisation. Addit. Manuf. **34**, 101360 (2020). https://doi.org/10.1016/j.addma.2020.101360
30. N.P. Calta, V. Thampy, D.R.C. Lee, A.A. Martin, R. Ganeriwala, J. Wang, P.J. Depond, T.T. Roehling, A.Y. Fong, A.M. Kiss, Cooling dynamics of two titanium alloys during laser powder bed fusion probed with in situ X-ray imaging and diffraction. Mater. Des. **195**, 108987 (2020)
31. S.M.H. Hojjatzadeh, N.D. Parab, Q. Guo, M. Qu, L. Xiong, C. Zhao, L.I. Escano, K. Fezzaa, W. Everhart, T. Sun, Direct observation of pore formation mechanisms during LPBF additive manufacturing process and high energy density laser welding. Int. J. Mach. Tools Manuf. **153**, 103555 (2020)
32. L. Zhou, H. Hyer, S. Thapliyal, R.S. Mishra, B. McWilliams, K. Cho, Y. Sohn, Process-dependent composition, microstructure, and printability of Al–Zn–Mg and Al–Zn–Mg–Sc–Zr alloys manufactured by laser powder bed fusion. Metall. Mater. Trans. A **51**, 3215–3227 (2020)
33. A. Sarangan, Physical and Chemical Vapor Deposition, in *Nanofabrication Principles to Laboratory Practice* (CRC Press, Boca Raton, 2016), p. 53. https://doi.org/10.1201/9781315370514-4
34. M.K. Zadeh, M. Yeganeh, M.T. Shoushtari, H. Ramezanalizadeh, F. Seidi, Microstructure, corrosion behavior, and biocompatibility of Ti–6Al–4 V alloy fabricated by LPBF and EBM techniques. Mater. Today Commun. **31**, 103502 (2022)
35. J. Yang, H. Yu, J. Yin, M. Gao, Z. Wang, X. Zeng, Formation and control of martensite in Ti–6Al–4V alloy produced by selective laser melting. Mater. Des. **108**, 308–318 (2016). https://doi.org/10.1016/j.matdes.2016.06.117
36. C.R.M. Afonso, G.T. Aleixo, A.J. Ramirez, R. Caram, Influence of cooling rate on microstructure of Ti–Nb alloy for orthopedic implants. Mater. Sci. Eng. C **27**, 908–913 (2007). https://doi.org/10.1016/j.msec.2006.11.001
37. G. Lütjering, J.C. Williams, *Titanium* (Springer Berlin, Heidelberg, 2007). https://doi.org/10.10007/978-3-540-71398-2
38. A. Carrozza, S. Lorenzi, F. Carugo, S. Fest-Santini, M. Santini, G. Marchese, G. Barbieri, F. Cognini, M. Cabrini, T. Pastore, A comparative analysis between material extrusion and other additive manufacturing techniques: defects, microstructure and corrosion behavior in nickel alloy 625. Mater. Des. **225**, 111545 (2023)
39. L. Bai, C. Gong, X. Chen, J. Zheng, L. Xin, Y. Xiong, X. Wu, M. Hu, K. Li, Y. Sun, Quasi-static compressive responses and fatigue behaviour of Ti–6Al–4 V graded lattice structures fabricated by laser powder bed fusion. Mater. Des. **210**, 110110 (2021)
40. A.M. Vilardell, A. Takezawa, A. du Plessis, N. Takata, P. Krakhmalev, M. Kobashi, I. Yadroitsava, I. Yadroitsev, Topology optimization and characterization of Ti6Al4V ELI cellular lattice structures by laser powder bed fusion for biomedical applications. Mater. Sci. Eng. A **766**, 138330 (2019). https://doi.org/10.1016/j.msea.2019.138330
41. A.M. Kamat, Y. Pei, An analytical method to predict and compensate for residual stress-induced deformation in overhanging

regions of internal channels fabricated using powder bed fusion. Addit. Manuf. **29**, 100796 (2019)
42. P. Promoppatum, R. Srinivasan, S.S. Quek, S. Msolli, S. Shukla, N.S. Johan, S. van der Veen, M.H. Jhon, Quantification and prediction of lack-of-fusion porosity in the high porosity regime during laser powder bed fusion of Ti–6Al–4V. J. Mater. Process. Technol. **300**, 117426 (2022)
43. J. Elambasseril, S.L. Lu, Y.P. Ning, N. Liu, J. Wang, M. Brandt, H.P. Tang, M. Qian, 3D characterization of defects in deep-powder-bed manufactured Ti–6Al–4V and their influence on tensile properties. Mater. Sci. Eng. A **761**, 138031 (2019)
44. R. Shi, S. Khairallah, T.W. Heo, M. Rolchigo, J.T. McKeown, M.J. Matthews, Integrated simulation framework for additively manufactured Ti–6Al–4V: melt pool dynamics, microstructure, solid-state phase transformation, and microelastic response. Jom **71**, 3640–3655 (2019)
45. M.V. Pantawane, Y.H. Ho, S.S. Joshi, N.B. Dahotre, Computational Assessment of Thermokinetics and Associated Microstructural Evolution in Laser Powder Bed Fusion Manufacturing of Ti6Al4V Alloy. Sci. Rep. **10**, 7579 (2020). https://doi.org/10.1038/s41598-020-63281-4
46. A.V. Gusarov, T. Laoui, L. Froyen, V.I. Titov, Contact thermal conductivity of a powder bed in selective laser sintering. Int. J. Heat. Mass. Transf. **46**, 1103–1109 (2003)
47. M. Godara, J. Joshy, B. Kuriachen, K.P. Somashekar, J. Mathew, Finite Element Analysis of Drilling on LPBF-Produced Maraging Steel, in *Advances in Forming, Machining and Automation: Select Proceedings of AIMTDR 2021*, ed. by U.S. Dixit, M. Kanthababu, A. Ramesh Babu, S. Udhayakumar (Springer, Singapore, 2023). pp. 319–329